Correlative light and electron microscopy : strategies and applications

Driel, L.F. van

Citation

Driel, L. F. van. (2011, October 11). *Correlative light and electron microscopy : strategies and applications*. Retrieved from https://hdl.handle.net/1887/17922

Chapter 4

Tools for Correlative Cryo-Fluorescence Microscopy and Cryo-Electron Tomography Applied to Whole Mitochondria in Human Endothelial Cells

Linda F. van Driel, Jack A. Valentijn, Karine M. Valentijn, Roman I. Koning, Abraham J. Koster

Department of Molecular Cell Biology, Section Electron Microscopy, Leiden University Medical Center, Leiden, The Netherlands

European Journal for Cell Biology
88(11):669-84. 2009.

Abstract

Cryo-electron tomography (cryo-ET) allows for the visualization of biological material in a close-to-native state, in three dimensions and with nanometer scale resolution. However, due to the low signal-to-noise ratio inherent to imaging of the radiation-sensitive frozen-hydrated samples, it appears oftentimes impossible to localize structures within heterogeneous samples. Because a major potential for cryo-ET is thereby left unused, we set out to combine cryo-ET with cryo-fluorescence microscopy (cryo-FM), in order to facilitate the search for structures of interest. We describe a cryo-FM setup and workflow for correlative cryo-fluorescence and cryo-electron microscopy (cryo-CLEM) that can be easily implemented. Cells are grown on finder grids, vitally labeled with one or two fluorescent dyes, and vitrified. After a structure is located by cryo-FM (with 0.4 µm resolution), its image coordinates are translated to cryo-ET stage coordinates via a home-built software routine. We tested our workflow on whole mount primary human umbilical vein endothelial cells. The correlative routine enabled us to investigate mitochondrial ultrastructure for the first time on intact human mitochondria, and led us to find mitochondrial cristae that were connected to the intermembrane space via large slits, which challenges the current view that such connections are established exclusively via small circular pores. Taken together, this study emphasizes that cryo-CLEM can be a routinely used technique that opens up exciting new possibilities for cryo-ET.

Introduction

Cryo-electron tomography (Cryo-ET) is rapidly expanding in the life sciences as a technique that allows for high-resolution 3D imaging of biological samples in a close-to-native state of preservation (Koster et al., 1997; Leis et al., 2008). Samples for cryo-ET are immobilized by rapid cooling down to cryogenic temperatures. The rapid cooling, which can be achieved for instance by high-pressure freezing or by plunge-freezing in liquid-nitrogen-cooled ethane, vitrifies the water in and around the sample. If a sample is thin enough (up to a few hundred nanometers), it can be viewed directly by cryo transmission electron microscopy (cryo-EM) and submitted to cryo-ET without any further processing (for a review, see Koning and Koster, 2009). Thus, the technique has been applied to several thin mammalian cell types (Briegel et al., 2008; Cyrklaff et al., 2007; Koning et al., 2008; Kurner et al., 2004). If samples are thicker, additional processing is required, such as cryo-ultramicrotomy (Al-Amoudi et al., 2004) or focused ion beam milling (Marko et al., 2007). Contrast in cryo-EM and cryo-ET is provided by local differences in molecular density of the sample. As a consequence, the differential contrast is much lower than in chemically fixed samples where contrast is improved by post-fixation and staining with electron-dense heavy atoms (e.g. osmium, uranium, lead). The low differential contrast is worsened by the low electron-dose requirements inherent to the technique. For the localization of structures of interest in cryo-EM, the lack of contrast is not a problem when the sample under investigation consists of a homogeneous population of structures, so that any area in the sample will be equally suitable for cryo-ET. It can become problematic, however, when a sample is heterogeneous in one or more aspects. To give but three examples, i) a sample can consist of cells that were genetically modified but only a subpopulation expresses the modification, ii) the features of interest can be infrequently occurring or short-lived events and therefore difficult to capture and find, or iii) a sample can contain thicker and thinner parts, only the latter being thin enough for cryo-ET. In scenarios like these, it is not uncommon that one can determine only after tomographic reconstruction whether an appropriate area of interest was recorded. It would therefore be extremely helpful if cryo-ET could be preceded by an imaging technique that does not cause radiation damage but allows for the pinpointing of areas of interest for subsequent cryo-ET. A technique that could achieve this is correlative light and electron microscopy (CLEM).

CLEM refers to a series of techniques that aim at correlating light microscopic images with electron microscopic images acquired from exactly the same location in a sample (J. A. Valentijn et al., 2009). Although CLEM studies have been published for over three decades, recent advances in fluorescence microscopy techniques, live-cell imaging, and fluorescent probe development have rekindled interest in CLEM research. The primary purpose of CLEM is to combine the advantages of light microscopy (generates overviews, large palette of stains and labels available, time-lapse recording) with those of electron microscopy (imaging at nanoscale resolution and in 3D (Koster and Klumperman, 2003)). Thus it becomes possible to study the dynamics of a biological process and subsequently identify the ultrastructural determinants underlying that process (van Rijnsoever et al., 2008; Verkade, 2008). In addition, CLEM can greatly facilitate the identification of areas of interest for ultrastructural analysis in complex samples (Agronskaia et al., 2008; van Driel et al., 2008; Vicidomini et al., 2008). To have this option available for cryo-ET, it is necessary that the light microscopy be performed at cryogenic temperatures. Because standard light microscopes are not designed for working at cryogenic temperatures, special equipment is required. Furthermore, an accompanying cryo-CLEM workflow is needed to keep the sample vitrified at all times during the procedure, and to establish a multimodal coordinate system for fast retrieval of areas of interest.

Recently, two separate cryo-CLEM approaches have been described in the literature, each including a home-made cryo-FM setup (Sartori et al., 2007; Schwartz et al., 2007). Here, we report our approach to cryo-CLEM, which was developed in parallel. Our cryo-FM setup is centered around a commercially available heating and freezing stage that can be mounted on any conventional upright light microscope. Only two modifications made it suitable for use in cryo-CLEM: i) the stage's specimen holder was adapted for carrying EM grids with vitreous samples, ii) a specimen loading box filled with liquid nitrogen vapor was attached to the stage to minimize frost buildup during grid transfers. Finder grids were used to provide reference points, and a coordinate translation routine was developed in Matlab to retrieve in cryo-EM structures of interest that were selected in cryo-fluorescence mode. The resolution of the cryo-fluorescence optics (0.4 µm) as well as the positioning accuracy of the translation routine (0.5 µm) are superior in comparison with the earlier reports. Thus, we believe that our approach excels in ease of implementation, convenience in use, and resolution of the cryo-fluorescence setup.

Using our cryo-CLEM approach, we examined, for the first time in primary human cells, the 3D ultrastructure of intact (i.e. non-sectioned) and fluorescently labeled mitochondria. Our results challenge the current view on mitochondrial membrane architecture: whereas the lumina of cristae are thought to connect to the inter-membrane space only via small circular openings, we show that the openings can also be elongated and slit-like.

Materials and Methods

Sample preparation

Human Umbilical Vein Endothelial Cells (HUVECs; Lonza, Walkersville, USA) were cultured as described previously (K. M. Valentijn et al., 2008). Briefly, cells were grown in Endothelial Growth Medium-2 (EGM-2; Lonza) on gold EM finder grids (Agar Scientific, Essex, England). The grids were of type HF15 (135 mesh) or type H6 (100 mesh) and were coated with Formvar and carbon. Prior to cell culture, grids were sterilized under UV light for 15 minutes. The cells were left to grow in standard cell culture conditions until they reached 70% confluence, which usually took 5 to 6 days; the culture medium was refreshed three times per passage. Up to 5 passages were used for experiments.

For vital labeling, cells were incubated 10 minutes in incubation medium containing 2.5 µM of the nucleic acid dye SYTO 59 (Molecular Probes, Leiden, the Netherlands). In dual label experiments, the medium containing SYTO 59 was replaced with HEPES medium (recipe according to (Romani de Wit et al., 2003)) containing anti-von Willebrand Factor (VWF) antibodies coupled to FITC (1:200; Abcam, Cambridge, UK) to label VWF that was released from the cells upon exocytosis. To induce exocytosis, the secretagogue phorbol myristate acetate (PMA) was also added to the medium at a concentration of 80 nM (50 ng/ml). After 20 minutes of stimulation, grids containing the cells were cryo-immobilized using a custom built plunge-freezing apparatus in which the grids were first blotted for one second at 37°C and ~100% humidity, and subsequently plunged into liquid ethane. Plunge-frozen cells were stored in liquid nitrogen until further use.

Temperature measurements

The temperature of the vitrified specimen during transfer and cryo-fluorescence imaging was monitored using a thin (0.25 mm) thermocouple (Thermo Electric, Waddinxveen, the Netherlands) that was attached to the sample grid. Temperature was recorded using a Voltcraft (Oldenzaal, the Netherlands) digital thermometer. Prior to performing the measurements, the thermocouple and thermometer ensemble was calibrated for a temperature range of -196°C to 20°C ±0.2%.

Cryo-fluorescence microscopy

Plunge-frozen grids containing fluorescently labeled HUVECs were imaged on a fluorescence microscope equipped with a THMS 600 freezing stage (Linkam, Surrey, UK). The stage and the specimen loading system were adapted to keep the specimen vitrified and free of ice contamination during the whole procedure (see Results for further details). Over the course of this study, we used the resulting cryo stage in conjunction with two different fluorescence microscopes: a Leitz DMRB (Leica, Wetzlar, Germany), and a Leitz Ergolux AMC (Leica). However, all data presented herein were acquired with the Leica DMRB microscope, which was equipped with a 100x dry objective without coverslip correction, and with a numerical aperture (NA) of 0.75, and a working distance of 4.7mm. Digital images were recorded with a Leica DFC350FX CCD camera, and a vario-zoom adapter was added to multiply the magnification of the objectives used by a factor of 0.55 to 1.1. Following cryo-FM imaging, sample grids were stored in liquid nitrogen until they were used for cryo-EM.

Resolution Measurements

To measure the optical resolution of the cryo-FM setup, we used yellow/green fluorescent beads with a subresolution diameter of 0.2 µm (Polysciences, Eppelheim, Germany). A drop of the bead-solution was brought onto an EM-grid, plunge-frozen into liquid ethane as described above, and imaged using the 100x dry objective with 0.75 NA. From six fluorescent micrographs, 22 single beads were selected that were well separated from others. Of each bead, the intensity profile was plotted in both x-and y-direction using imageJ (Abramoff, 2004). To be able to compare the intensity profiles, we fitted a Gaussian curve through all 44 plots, and normalized them to the maximum and minimum values of the Gaussian fits. The resolution was then determined by measuring the full width at half maximum (FWHM) of the corrected plots.

Cryo- electron microscopy and image analysis

The grids that were imaged in cryo-FM mode were prepared for cryo-EM by transferring them into an EM cryo-holder type 626 (Gatan, Pleasanton, USA). The microscope used was a Tecnai F20 FEG (FEI, Eindhoven, the Netherlands), operating at 200kV. Images were recorded with a 2k x 2k camera with energy filter (Gatan 2002). The coordinates of the LM images were translated to the new coordinates in the EM with a home-built Matlab script performing an affinity matrix transform. In this script, the EM coordinates of four known points in the LM image, for example the grid bar corners, were collected, and the script then calculated the coordinates of the region of interest (for details, see the Results section).

For cryo-electron tomography, 15 nm colloidal gold particles were used as fiducial markers. They were added to the carbon side of the EM support grids prior to cell culture. Tilt series were acquired using Xplore 3D software (FEI). For the tomogram shown in Fig. 7, the tilt series was recorded at a defocus of -15 µm, over an angular range of 90˚ (-50 to + 40) with 2˚ increments, and with a resulting pixel size of 0.8 nm.

Tomographic tilt series were processed using the IMOD software package, and filtered by anisotropic diffusion to reduce noise while preserving edges and contrast (Kremer et al., 1996).

Image stitches and overlays of FM/EM images were made using Adobe Photoshop CS3 (San Jose, California).

Results

The goal of the present study was to develop a setup and workflow for cryo-CLEM that permits visualization of structures in cryo-FM at subcellular resolution, and that retrieves those structures accurately in cryo-EM for the purpose of tomography. We aimed at a cryo-fluorescence setup that was easy to implement. In this spirit we opted for a commercially available heating and freezing stage (Linkam THMS 600), which we modified in order to accommodate EM support grids. The workflow we designed is summarized in Fig. 1, and the cryo-fluorescence setup in Fig 2.

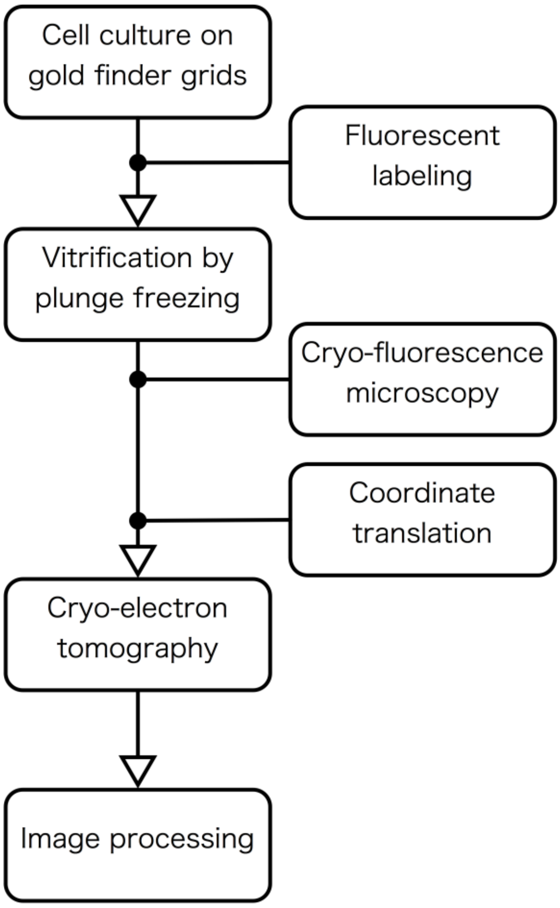

Figure 1: Schematic representation of the cryo-CLEM workflow described in this study. The left column depicts the standard workflow for cryo-ET, while the intercalated boxes on the right hand indicate the additional actions that are required for cryo-CLEM.

The cryo-FM stage: modifications and performance

Although the THMS 600 was designed with applications in mind that necessitate rapid temperature changes between -196 and 600 °C, it also met several of the requirements we specified for a cryo-LM stage: it can maintain a specimen at the temperature of liquid nitrogen over long periods of time, the specimen chamber is air-tight and flushed with cold, dry nitrogen gas to prevent frost build-up, a specimen can be viewed by both bright-field and fluorescence microscopy, the stage can be mounted on any conventional, upright microscope, and the stage is compatible with high numerical aperture (NA) objectives, which usually operate at short working distances.

The specimen is mounted on a silver heating/cooling element, the surface of which is polished for optimal heat or cold conduction. A pump draws liquid nitrogen from a Dewar and injects the liquid nitrogen into the silver block. The evaporated nitrogen is recycled and used to purge the specimen chamber. The temperature of the silver block is monitored with a platinum resistor sensor and regulated by means of a temperature controller. A small hole in the middle of the silver block allows for transillumination of the specimen for widefield microscopy. A schematic drawing and photographs of the setup are shown in Fig. 2A through 2C.

The stage was designed to hold a specimen on a round glass coverslip that is clamped in a stainless steel specimen-loading cartridge. The cartridge can be inserted into the specimen chamber via a side-entry port. For the purpose of cryo-CLEM, it was necessary to modify the specimen transfer system to allow for specimen loading under liquid nitrogen. Therefore we replaced the glass coverslip area of the cartridge with a thin (0.8 mm) brass disc. The brass not only provided proper support for the EM grid, but also acted as a cold sink during transfer of the cartridge from the liquid nitrogen bath (used for grid loading) onto the silver block in the freezing stage. For the positioning of EM grids, a circular depression with a diameter of 3 mm was milled in the center of the brass disc. The grid was held in place by a pivoting clamp mechanism that was taken from a specimen holder for room temperature EM, and mounted onto the stainless steel loading cartridge. Forceps were used to open and close the clamp mechanism under liquid nitrogen (supplementary material 1). The modified specimen cartridge is shown in Fig. 2D.

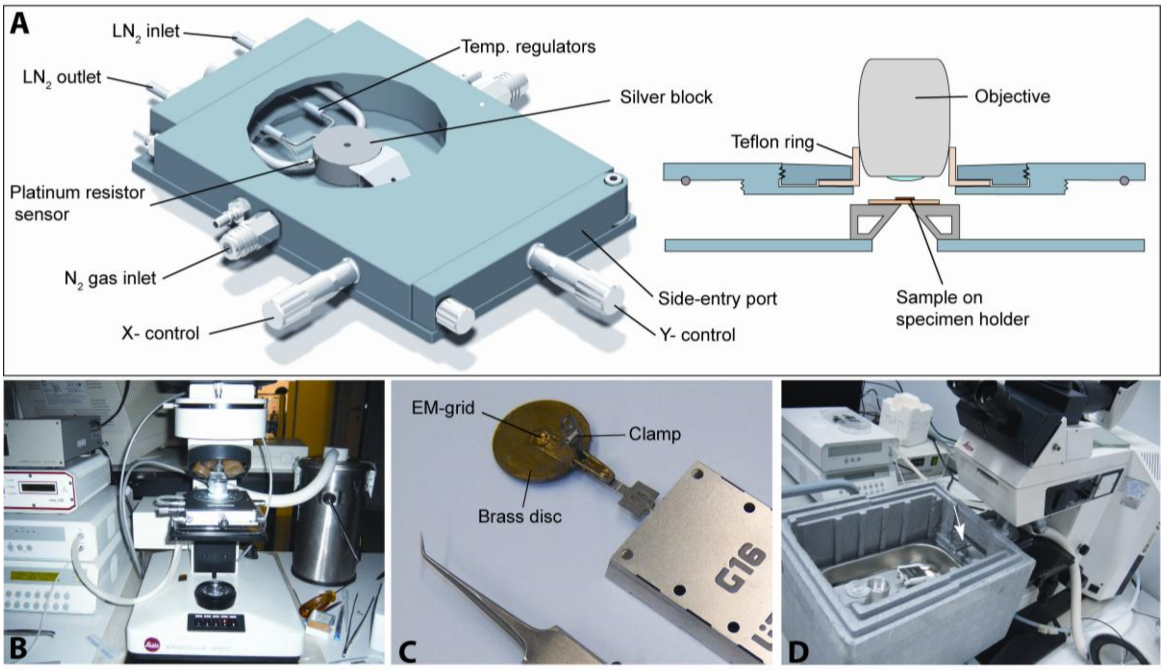

Figure 2: The cryo-fluorescence setup. (A) 3D rendering of the freezing stage without a lid, and schematic cross section through the teflon ring lid and silver block. (B) Photograph of the set-up with accessory devices mounted on a Leitz fluorescence microscope. The nitrogen Dewar on the right of the microscope is connected to the stage via an insulated tube. The temperature controller and nitrogen pump are shown on the left hand side, bottom unit and second from the bottom unit, respectively. (C) Modification of the specimen cartridge to enable loading of EM grids. The forceps serves to open and close the clamp. See text for further details. (D) Styrofoam box construction used to minimize frost-buildup during specimen transfer to and from the freezing stage. A small window (arrow) cut in one of the sides of the Styrofoam box slides over the side-entry port of the freezing stage. A stainless steel basin placed on the bottom of the Styrofoam box is used to attach a Teflon holder in which the specimen cartridge can be secured during loading and unloading of a EM grid. See text for further details. Notice that the freezing stage is mounted on a different microscope (Leica DMR) than the one shown in Fig. 2B.

Because air humidity levels in our laboratory are typically around 70%, transfer of the specimen cartridge through the air would inevitably result in ice contamination of the cold specimen. Therefore we experimented with different strategies to reduce the risk of frost buildup during transfer of the specimen into and out of the freezing stage. To give an example, we constructed a sealed Perspex box over the microscope and pressurized the box with a constant flow of nitrogen gas in order to lower the humidity level in the transfer area (J.A. Valentijn et al., 2008). Although this setup brought the humidity level down to 10%, it rendered the sample loading via armholes cut in the box so impractical that the vitreous state of the specimen was often compromised. The most effective approach, which we incorporated in the final setup, was to slide a Styrofoam box over the side-entry port of the freezing stage (Fig. 2E). For this, a window the size of the freezing stage/side-entry port was cut out of one of the sides of the Styrofoam box. The Styrofoam box was filled with liquid nitrogen up to the lower border of the window. In the box lay a stainless steal bath that carries a compartment for a grid-storage box and a Teflon holder that can support the sample cartridge. This construction allowed for the rapid loading and unloading of the sample cartridge from the liquid nitrogen into the freezing stage, while frost buildup was counteracted by the gas flow of evaporating liquid nitrogen. We found that this construction greatly reduced the amount of ice crystals. A video recording of the specimen transfer is shown in supplementary material 1.

If the specimen temperature is allowed to rise above -130˚C during handling, crystalline ice will appear and damage the ultrastructure of the sample (Dubochet et al., 1988). This prompted us to monitor the influence of handling of the grid-loading cartridge on specimen temperature. Therefore we performed temperature measurements with a thin (0.25 mm) thermocouple seated in the EM grid enclosure (Fig. 3A). We then handled the holder as if a grid was carried, and recorded the temperature during operation, both of the thermocouple and silver block (for the latter using the built-in platinum resistor electrode). A typical example of the temperature fluctuations we measured over the course of the whole procedure is shown in Fig. 3B. When in liquid nitrogen, the thermocouple registered around −196˚C. During loading of the holder into the stage, usually lasting 6 seconds, the temperature did not deviate from this value. Neither did it rise, after loading in the freezing stage, when the holder was moved in X- and Y-directions, or when the grid area was irradiated with fluorescent light. Only the process of removing the holder from the stage, normally lasting approximately 10 seconds, led to a small rise in temperature, up to -190˚C. This rise reflected a relatively slow change, owing to the brass base of the holder, which served as a cold mass. To determine how long a transfer could actually last before reaching the critical temperature of -130˚C, we measured the change in temperature upon removing the holder from liquid nitrogen and keeping it at room temperature. The thus obtained temperature recordings revealed that -130 °C was reached in as much as 25 seconds (dashed line in Fig. 3B), indicating that the time needed for loading (3 s) and unloading (6 s) was well within the safe range for maintaining the specimen in a vitrified state.

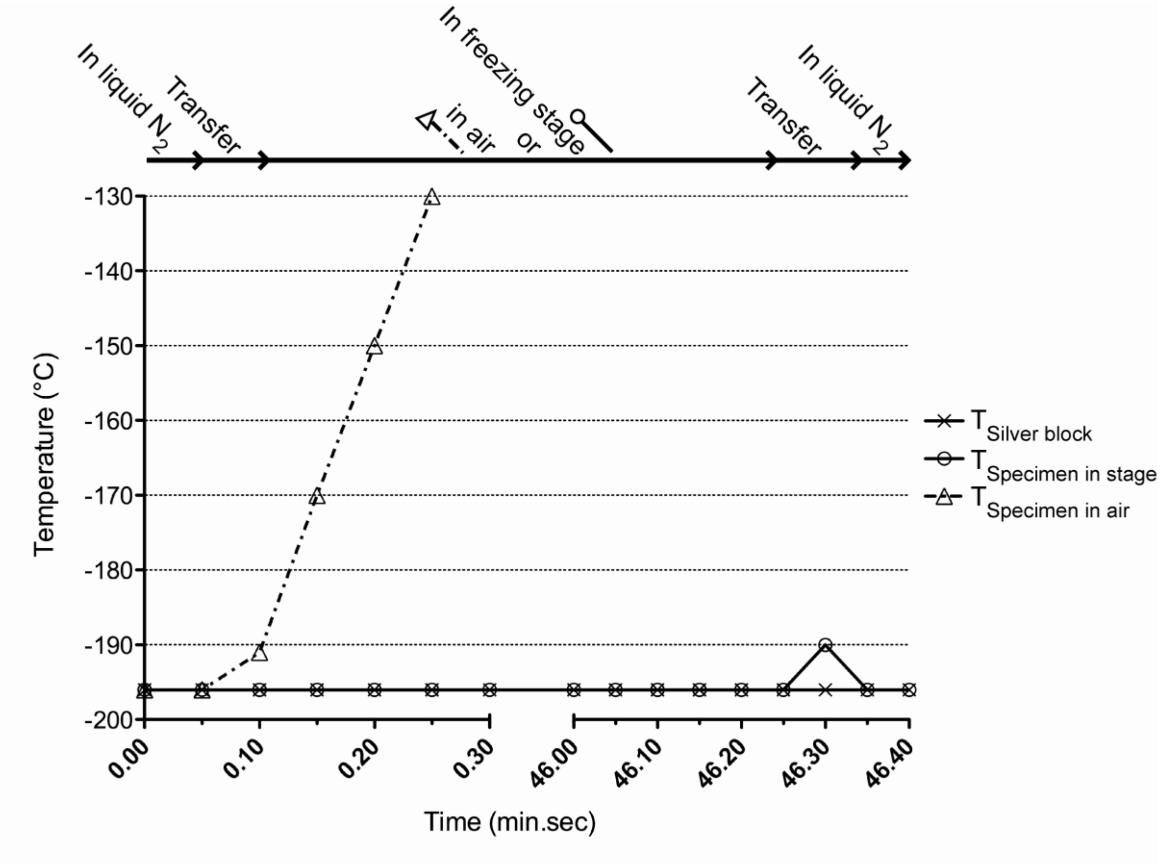

Figure 3: Efficiency of the modified freezing stage, the cryo stage, in maintaining temperature. The graph shows a typical set of temperature measurements that were performed to examine the specimen temperature over time in the cryo stage and during critical transfer steps. Upon transferring the specimen cartridge from liquid nitrogen to ambient air (room temperature), it took 25 s for the specimen to reach -130 °C (dashed curve), a critical temperature at which devitrification of biological samples sets in. Cryo stage loading and unloading of the specimen cartridge (solid curves), which typically lasted 10 s or less, caused little or no temperature fluctuations.

Besides modifying the freezing stage to meet the requirements for cryo-LM, i.e. temperature maintenance and minimization of ice contamination, we also aimed for a high lateral resolution of the cryo-fluorescence imaging. Only at a relatively high resolution (>0.5 µm) one can identify subcellular features such as lysosomes, mitochondria, secretory vesicles, and junctional complexes. The subcellular features may either constitute the subject of investigation, or provide visual clues for pinpointing regions of interest; in either case, it emphasizes the notion that the visualization of subcellular detail by cryo-fluorescence microscopy is an important goal for cryo-CLEM. In order to obtain sufficiently high resolution, we strove for an uninterrupted light path between the objective and the specimen. We achieved this by replacing the insulating glass window on the freezing stage with a Teflon objective collar. In addition, we opted for a dry (i.e., non-immersion) objective without coverslip correction. The objective we chose for imaging had a magnification of 100X, yielding a relatively small field of view of 90 by 90 µm. However, it was often desirable to have larger microscopic overviews to facilitate the retrieval of areas of interest at the cryo-EM. Because it was not possible to switch to a lower magnification objective, as it would inevitably compromise the specimen quality, we used a 0.55-1.1X vario-zoom adapter between the microscope and the CCD camera. This allowed us to acquire both overview and detail images with the same objective. The choice of the microscope objective was further dictated by the best possible compromise between two opposing requirements: a high numerical aperture (NA) to yield high-resolution cryo-fluorescence images and a long working distance to prevent temperature fluctuations of the specimen due to warmth irradiation from the objective. This compromise was found in an objective with a 0.75 NA and a 4.7 mm working distance. According to the equation $R = 0.61\lambda/NA$, where R is the resolution and λ is the imaging wavelength (488 nm), the theoretical resolution of the objective was 0.4 µm. Because temperature gradients and the vitreous water interface might affect the resolution of the objective, we determined the actual resolution by measuring the FWHM of intensity plots of subresolution fluorescent beads that were plunge-frozen and imaged in the cryo-FM stage (Fig. 4). The FWHM yielded a resolution of 0.4 ± 0.02 µm.

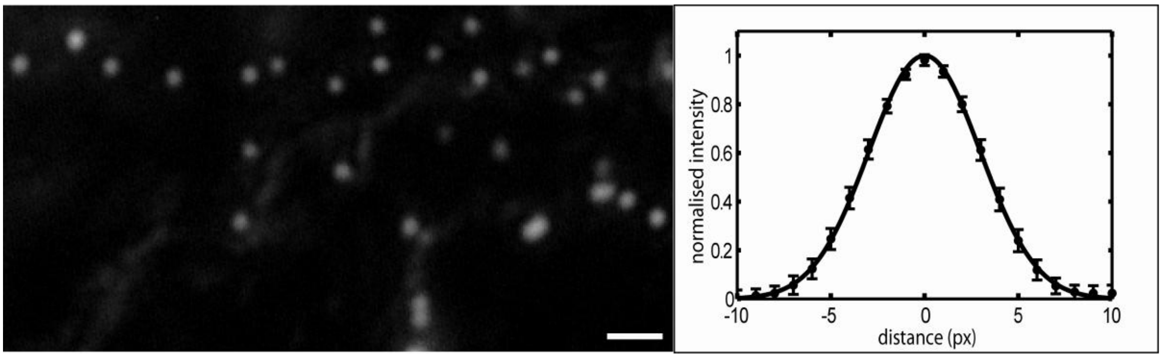

Figure 4: Lateral resolution measurement of the cryo-fluorescence optics. A cryo-fluorescence micrograph is shown of vitrified subresolution beads (diameter: 0.2 µm) made of polystyrene and yellow-green fluorescent. The graph shows the average Gaussian fit of the intensity profiles across 22 beads, normalized to their minimum and maximum intensity. The error bars represent the corresponding grey-value data. Scale bar represents 2 µm.

Coordinate matching between FM and EM imaging

As mentioned in the Introduction, frozen-hydrated specimens exhibit characteristic low contrast and high noise levels owing to the low electron dose requirements of cryo-EM. As a result, there was a lack of visual clues to retrieve in cryo-EM mode areas of interest that were selected in cryo-FM mode. This problem of visual correspondence was intensified by magnification differences between both imaging modes, and, most importantly, by the fact that the physical transfer of the specimen grid often resulted in rotation and mirroring of the sample (the latter occurring when the grid was flipped over). Therefore we set out to develop a coordinate translation method that relates the spatial coordinates of the fluorescence images to the coordinates of the goniometer.

For coordinate translation, visual landmarks need to be present in both imaging modes for providing positional and orientational clues. In our case, we made use of the unexpected observation in cryo-FM mode that the EM-grid bars were outlined by a fluorescent signal. Although this fluorescence appeared to be nonspecific, it only occurred in areas where specific fluorescence, i.e. of labeled cellular structures, was also present, suggesting that it resulted from a reflection of the specific fluorescence. In cryo-EM mode, the grid bars were also easily recognized because they blocked the electron beam. To facilitate the use of grid bar patterns as landmarks, we made use of commercially available finder grids in which grid squares were labeled with alphabetical characters whose edges also reflected fluorescence (Fig. 5).

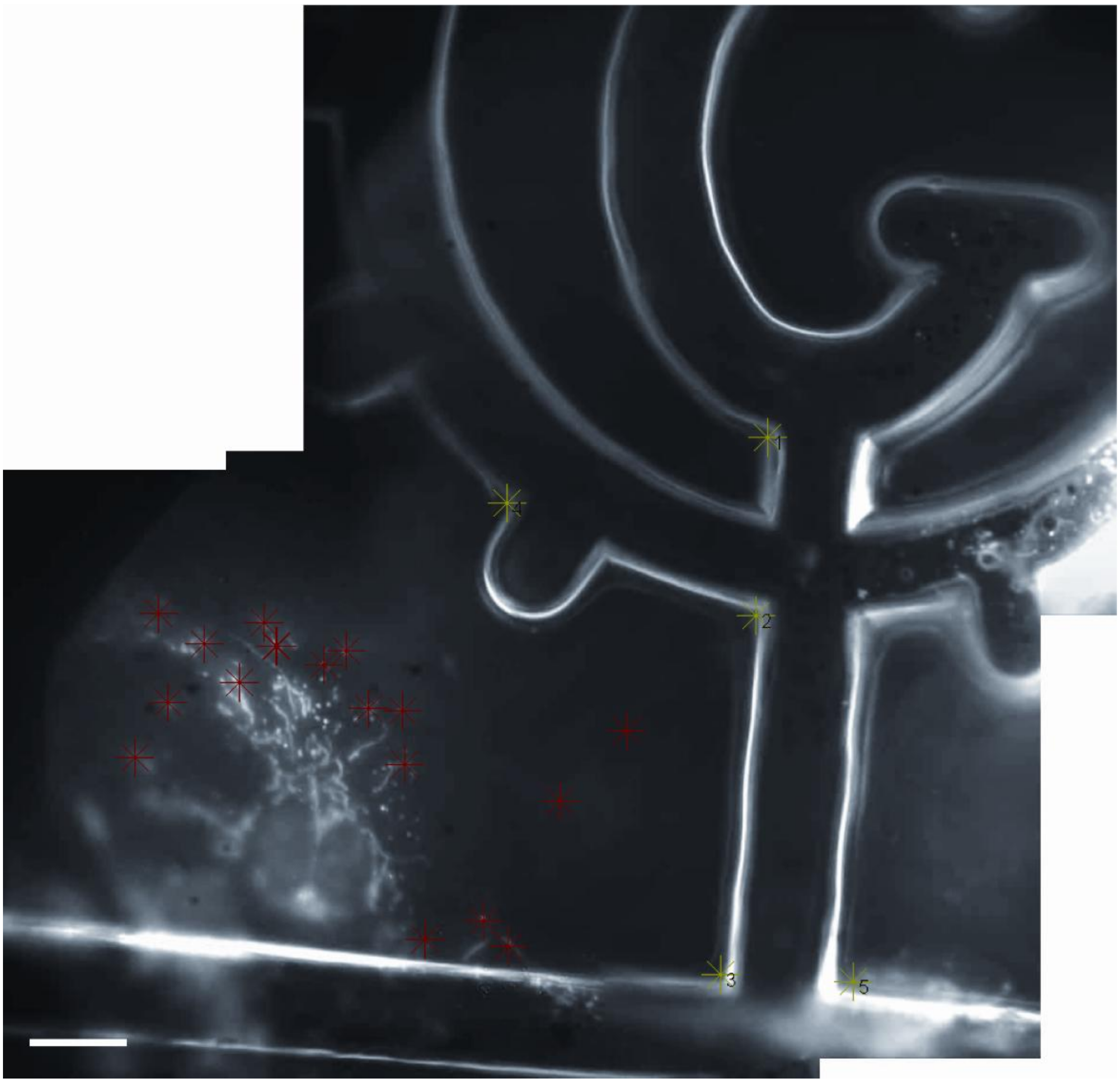

Figure 5: Implementation of the home-built routine for multimodal coordinate retrieval. Three cryo-fluorescence micrographs were stitched together to display part of a finder grid (containing the letter G) with fluorescently labeled cells. The green stars point at landmarks (grid bar corners) that are visible by both FM and EM. After locating and centering landmark 1, The EM user positioned a green star so that the software could register the x- and y- coordinates of that location. The user repeated this for 5 landmarks. Subsequently, red stars were tagged on locations where cryo-EM information was desired. Using the coordinates of the green stars, the software calculated the coordinates of the red stars, and directed the motorized EM stage controls to that location. Scale bar represents 20 µm.

Our coordinate translation method is a two-step approach, where global localization is succeeded by precise localization of structures of interest. In cryo-FM mode, image stitches of areas of interest were recorded that included the nearest character of the finder grid. Typically, a cryo-FM image stitch consisted of three to six digital FM images covering a relatively large area of about 500 by 500 µm. As a first step in the routine (global localization), the same grid character was located in cryo-EM at low magnification. We used a field of view that was about the size of a whole character (90 by 90 µm). The positioning accuracy provided by the finder grids was refined by the second step (precise localization), comprising a software routine, which was written in Matlab. We termed this software routine LCOTRAS, for Leiden COordinate TRAnslation Script. It determines the coordinate transform between the XY-controls of the EM mechanical stage and the XY-coordinates of the FM image containing the area of interest. Further details on usage of the script and its computing background are available as supplementary online material 2. The script will be made freely available to academic users upon request.

For the precise location of a given feature, the coordinate translation method needed to have an as high as possible spatial positioning accuracy. The positioning accuracy is linked to (i) the attained resolution of the fluorescence microscope and (ii) to the field of view that is acquired with the EM. The positioning accuracy should ensure that the area acquired with the EM will cover the areas corresponding to the fluorescent spot that was observed with the fluorescence microscope. With this definition it follows that

CCD field of view in EM > 2 * Resolution FM + Positioning accuracy

Given that the resolution of the FM was 0.4 µm, and that the EM field of view necessary to contain always the feature of interest was 1.3 µm2, it follows that the experimental positioning accuracy of our coordinate translation method was 0.5 µm. It therefore proved to be a reliable tool that rendered the electron exposure of a structure of interest prior to tomography neglegible.

The cryo-CLEM workflow in action

To demonstrate the feasibility of our cryo-CLEM workflow and its applicability to frozen-hydrated biological samples, we used Human Umbilical Vein Endothelial Cells (HUVECs) in which the mitochondria were fluorescently labeled. We found that HUVECs grow very thin in their peripheries, usually thinner than 100nm, allowing them to be used in toto for cryo-EM without the need of vitreous sectioning. The cells were grown on gold finder grids, vitally labeled with a cell-permeable stain (SYTO 59), and vitrified by plunge freezing. We then followed the cryo-CLEM workflow as described above.

A typical example of vitrified HUVECs submitted to the cryo-CLEM workflow is shown in Fig. 6. The cells were labeled with the nucleic acid dye SYTO 59, which yielded a predominantly mitochondrial staining-pattern. This pattern probably resulted from SYTO 59 binding to mitochondrial DNA. In cryo-FM mode, an image stitch was made to include several cells with their

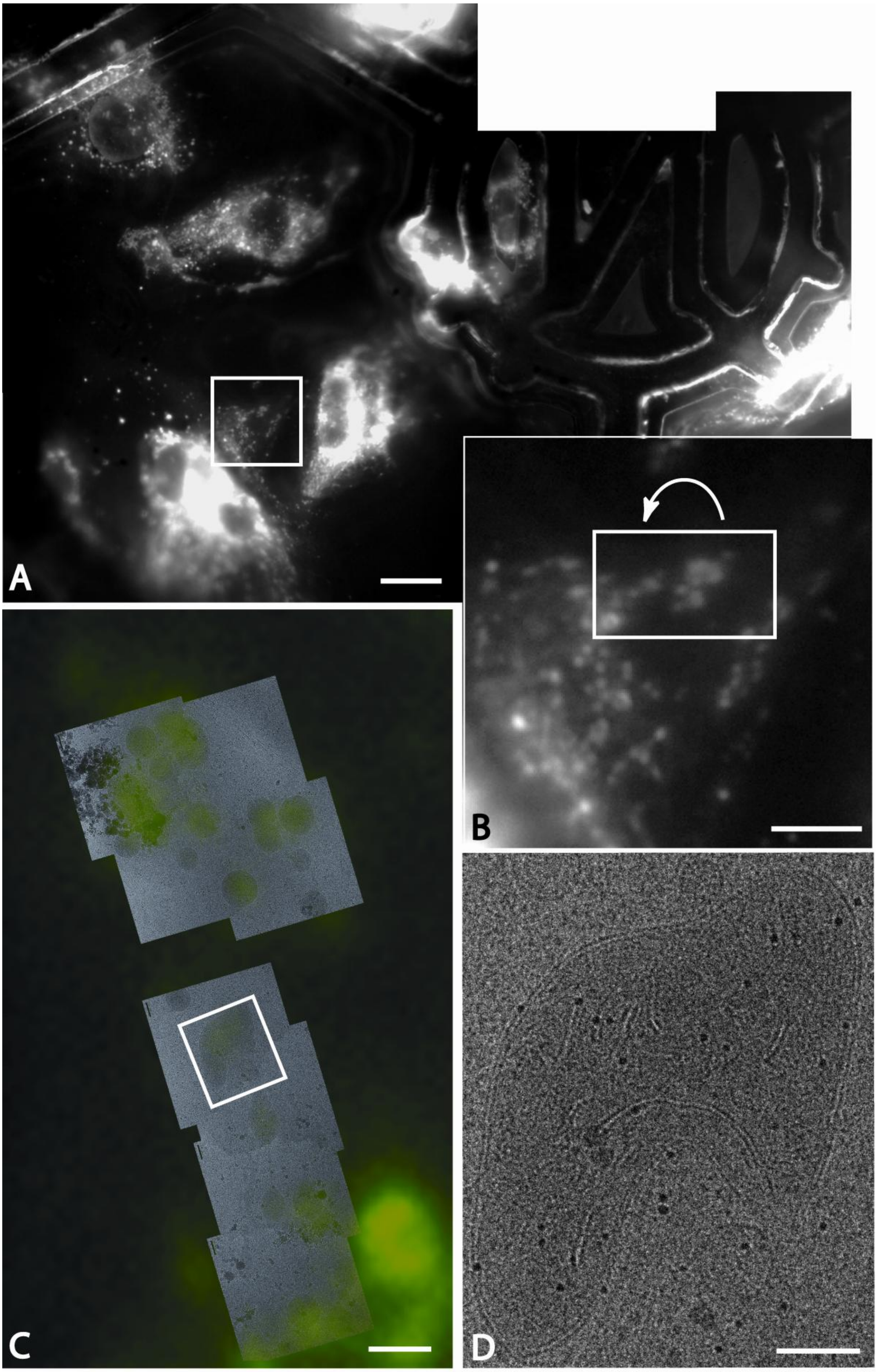
A
B
C
D

Figure 6: Using the cryo-CLEM procedure to localize and image mitochondria. (A) Cryo-FM overview of part of a mesh of a finder grid, showing several HUVECs that were grown on the support film. The cells were labeled vitally with SYTO 59, which in this cell type stained preferentially mitochondria. Note that the grid bars and the letter N of the finder grid are also visualized, presumably due to reflection of the SYTO 59 fluorescence. Overviews like this were used effectively to retrieve features of interest in subsequent cryo-EM mode. A zoom of the boxed area in (A) is shown in (B). Here, the resolving power of the cryo-fluorescence setup is such that individual mitochondria can be distinguished. Image (C) is a further zoom of the boxed area in (B), superimposed on a corresponding cryo-EM overview image. To aid in the visualization of the overlay, the fluorescence was colored red and made semi-transparent. The fluorescence now coincides with electron dense features in the EM overview. Some ice contamination is present in the upper left corner of the EM image. (D) Higher-magnification cryo-EM image of the boxed area shown in (C), revealing the ultrastructure of a mitochondrion. Its characteristic double membranes and cristae can be appreciated. Also visible are several 15-nm gold particles that were used as fiducial markers to reconstruct tomograms (not shown). Scale bars represent 10 µm in (A), 3 µm in (B), 1 µm in (C), and 200 nm in (D).

surrounding grid bars (Fig. 6A). The stitch was then used to pinpoint the peripheries of the cells and select mitochondria. In order to display the entire stitch, the images were scaled down. At native resolution, it appeared that separate mitochondria could be distinguished (Fig. 6B). This was corroborated subsequently in cryo-EM mode, where the same area of mitochondria was readily retrieved with the correlation script, using the stitched LM image as input to calculate the corresponding EM coordinates. An EM image stitch made of the same area, and overlaid with the corresponding fluorescence image, demonstrated clearly the correlation between the SYTO 59 signal and mitochondria, and thereby validated our approach (Fig. 6C,D).

Despite the precautions we took, some degree of ice contamination could not be avoided. However, even in the worst-case scenario, an example of which is shown in Fig. 7, ice contamination was manageable in that the ultrastructural integrity of features of interest could still be appreciated. Frost buildup remained undetected in cryo-FM mode (Fig. 7A,B), but was present in cryo-EM mode as small blobs with diameters up to 100 nm (Fig 7C,D). Because of their small size, mostly sparse distribution, and relative electron lucency, the contaminating ice crystals only mildly deteriorated the quality of the cryo-electron tomograms. This is illustrated in Fig 7E showing a digital slice through part of a mitochondrion of which a standard micrograph is shown Fig. 7D. The tomographic reconstruction revealed a bifurcating crista in an area where the sample was covered by a clump of four ice particles. Membrane delineations were easily traced and fine details, such as a macromolecular density in the lumen of the crista, were detectable (Fig. 7F). Digital sectioning of tomograms in the plane perpendicular to the imaging plane showed that the ice particles appeared to be peripherally deposited on top of the vitreous layer on the one side, and on top of the Formvar film on the other side of the specimen (Fig. 7F). Thus the frost contamination did not appear to compromise the vitreous layer containing the biological sample.

At the ultrastructural level, the mitochondria showed complex organization of their internal membranes, as shown in Fig. 7G and the movie in supplementary online material 3. The multiple

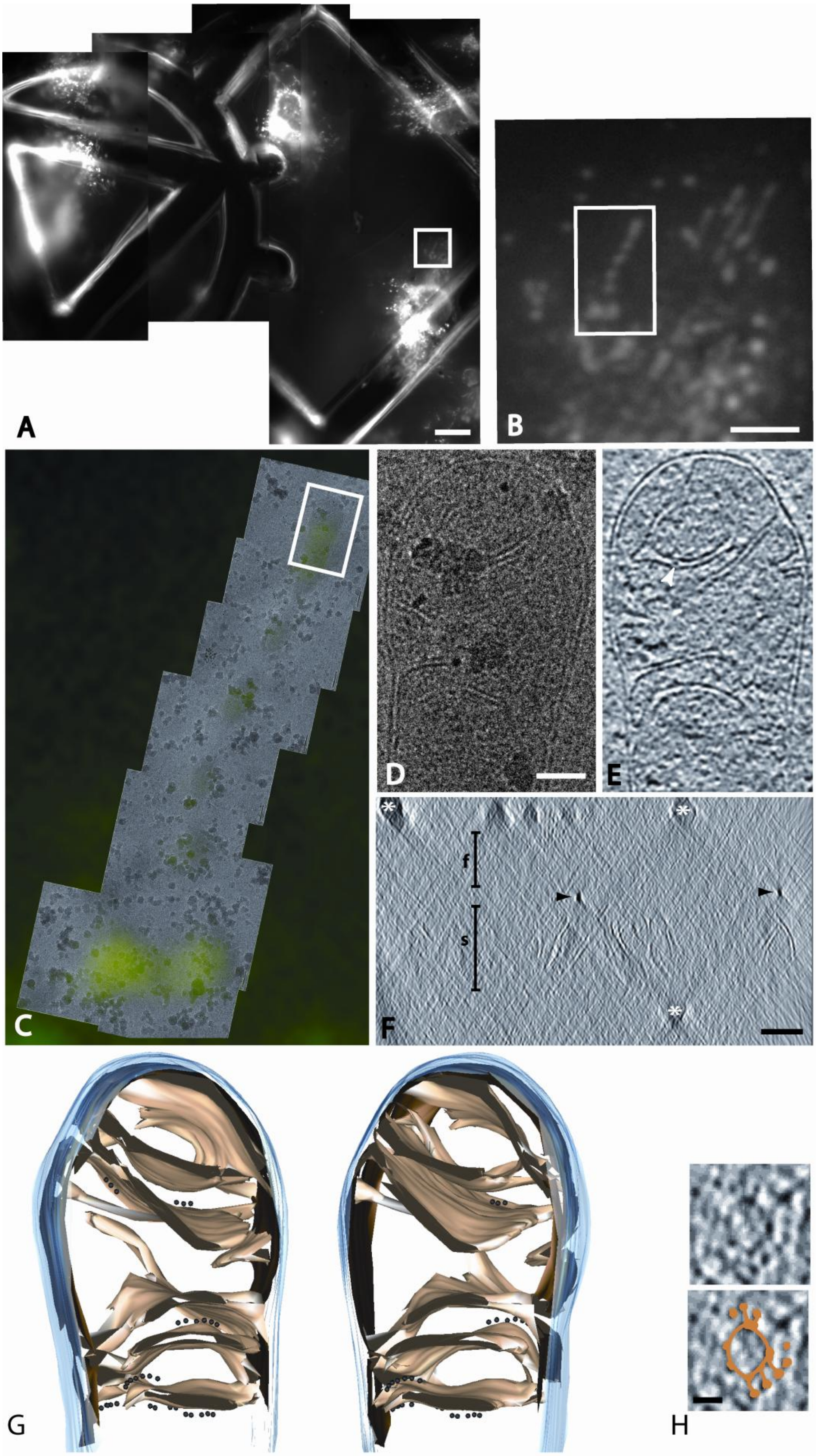
A
B
C
D
E
f
s
F
G
H

Figure 7: Combining cryo-CLEM and electron tomography. (A) Cryo-FM overview of SYTO 59 labeled HUVECs. A zoom of the boxed area in (A) is shown in (B). Numerous individual mitochondria are seen in this zoom, including a strand of mitochondria in the boxed area. The mitochondria in the boxed area were retrieved and imaged with cryo-EM. The resulting superimposed cryo-FM image and cryo-EM overview is shown in (C). Note that this sample displayed more ice contamination than the example shown in Fig. 7 (the ice crystals have the appearance of small electron-dense blobs spread out over the sample). (D) Higher magnification cryo-EM image of the boxed area in (C), containing part of a mitochondrion that correlated with the SYTO 59 fluorescence. Ice crystals mask several areas of the mitochondrion. However, as shown in (E), the ice crystals are no longer seen in digital slices through the mitochondrion following cryo-electron tomography, and they do not appear to interfere qualitatively with the tomographic reconstruction. The arrowhead points to a macromolecular density in the lumen of a bifurcating crista, an area that was covered by ice in the 2D cryo-EM image shown in (D). (F) Digital YZ slice through the tomogram shown in (E), revealing that the ice crystals are peripherally attached to the sample and support film. Several layers of material can be distinguished; from top to bottom: a layer of ice crystals (asterisk indicates one ice crystal), Formvar support film (f), gold particles used as fiducials (arrowheads), the vitreous sample (s), which can be recognized by the mitochondrial membranes, and again ice crystals (asterisk). Thus the ice crystals did not penetrate the sample, but have precipitated onto it. (G) Three-dimensional model of the mitochondrion from the tomogram in (E), shown at two different angles. The outer membrane is depicted in blue, the inner boundary membrane in dark brown, the cristae in light brown, and several ATP synthases in black. Notice that the cristae are disc-like rather than tube-like, and that the junctions of cristae with the inner membrane are often elongated. (H) The ATP-synthases drawn in (G) formed a pattern of repeating densities as shown in the top panel, sometimes connected by a stalk to dense regions in the membrane. In the lower panel, the same image is superimposed with a schematic representation of the putative ATPases. Scale bars represent 20 µm in figure (A), 5 µm in figure (B), 100 nm in figures (D) and (F), 10 nm in (H).

lamellar cristae bifurcated and fused with one another, and, in contrast to the current paradigm, the junctions where cristae and the inner boundary membrane joined were either circular or elongated (up to 120 nm long). Similarly elongated cristal openings were also observed in unlabeled mouse embryonic fibroblasts (a movie is available as supplementary online material 4). The outer and inner membranes of the mitochondria were separated by a uniform distance of about 8 nm, or 20 nm including both membranes, while the distance between opposing cristal membranes was somewhat variable but with a comparable mean distance of 8 nm excluding, and 20 nm including the membranes. In addition to membranes, many macromolecular densities were apparent, some of which resembled ATP-synthases, because they formed rows of densities with 5-nm long stalks emanating from the cristal membrane (Fig. 7H), features that have been attributed to ATP-synthases (Gruska et al., 2008; Nicastro et al., 2000).

Besides representing a good marker to localize mitochondria, we found the SYTO dye to be also very useful for providing landmarks that describe the general topology of cells. Because HUVECs have a ‘fried egg’ appearance, the thicker part where the nucleus is situated is too thick for electron imaging. The SYTO stain readily outlined the nuclear area as well as the periphery of HUVECs where the cells were thin enough to allow for electron tomography. Since the freezing stage was designed for compatibility with standard fluorescence microscopes, it was possible to perform dual-label fluorescence microscopy on the vitrified cells. An example of dual-label cryo-fluorescence microscopy is illustrated in Fig. 8. Here, sites of exocytosis on secretagoguechallenged HUVECs were detected with a FITC-conjugated antibody against VWF, which is the major secretory output of HUVECs (Babich et al., 2008). The fluorescent VWF antibody was used as a vital stain, i.e. it was added to the incubation medium during secretagogue stimulation. As can be seen in Fig. 8A, the pattern of VWF labeling provided little or no indication about the topology of the underlying HUVECs. This lack of orientation was remedied by double labeling with SYTO 59 (Fig. 8B), which made it possible to select those sites of exocytosis that were potentially suitable for electron tomography. Cryo-CLEM data on the ultrastructure of exocytosis sites and exocytosed VWF will be published in a separate paper (manuscript in preparation).

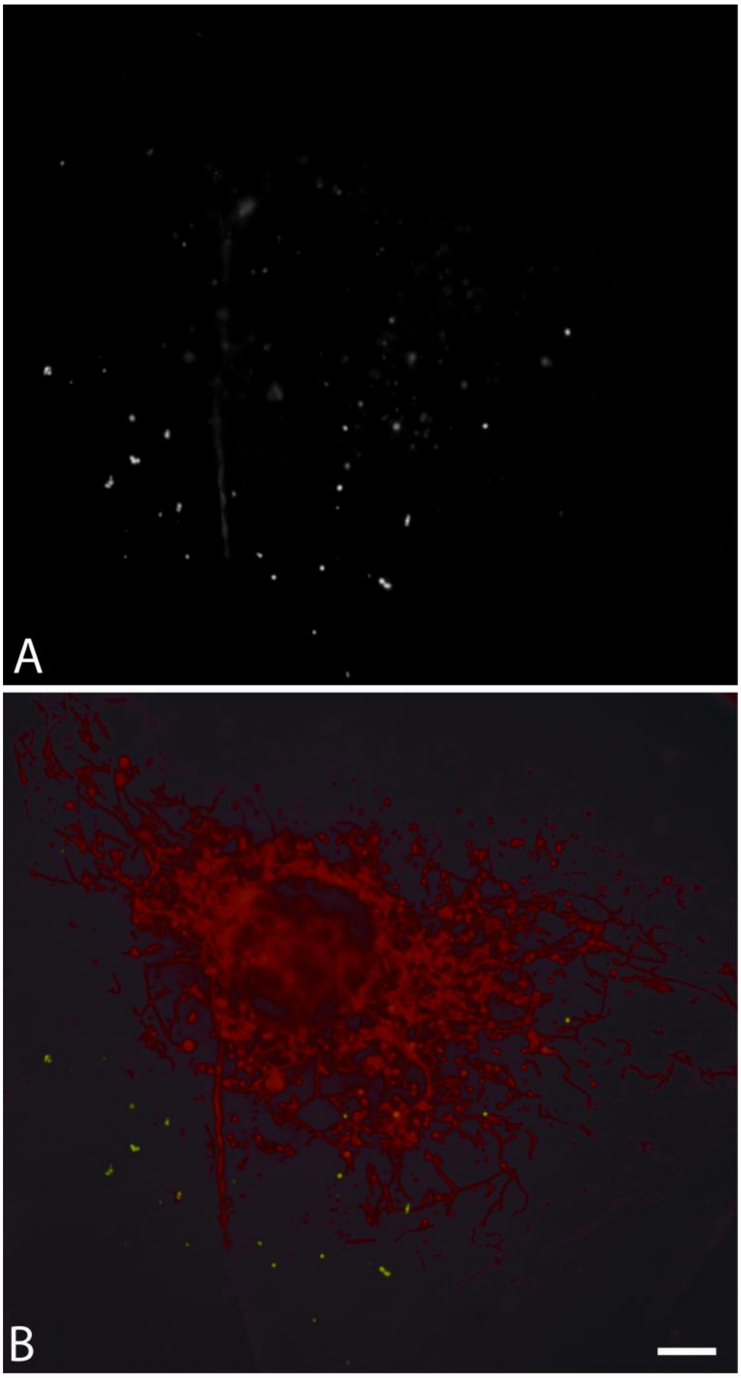

Figure 8: Dual label cryo-fluorescence microscopy. The SYTO 59 label was used to provide landmarks, thereby aiding in the quick EM retrieval of features of interest. (A) Cryo-FM image of a HUVEC that was stimulated to undergo regulated exocytosis in the presence of a FITC-conjugated antibody to VWF. The fluorescent antibody binds to VWF as it is secreted from the cells, and thereby marks locations of exocytosis, which have the appearance of bright fluorescent dots. Because the antibody only detected exocytosis sites, it did not provide visual cues that would allow for orientation in the context of the underlying cells. (B) Dual label cryo-FM image of the same area as in (A), but now showing the VWF label in green, and a SYTO 59 label in red. The SYTO 59 stain enabled orientation in the cell by defining the location of the nucleus and cell periphery. The vertical stripe that is visible in both the red and green channels represents nonspecific fluorescence due to a crack in the Formvar support film. Such artifacts were also used as landmarks for coordinate retrieval in cryo-EM mode. Scale bar represents 5 µm.

Discussion

The present report describes a complete cryo-CLEM workflow for the localization of features of interest by cryo-FM and their subsequent ultrastructural examination by cryo-EM and cryo-ET. We used human endothelial cells to demonstrate the applicability of the workflow. The cells were grown directly on EM grids, vitally labeled with one or two fluorescent probes, vitrified, and imaged in a cryo-FM stage. In cryo-EM mode, we used a coordinate translation program to retrieve the features of interest pinpointed by cryo-FM, and were thus able to obtain ultrastructural information of the fluorescent features. The main component of the methodology is a cryo-fluorescence microscope stage that allows viewing of frozen hydrated specimens.

Cryo-light microscopy (cryo-LM) in itself is not a new concept, as it has been used to study freezing and thawing processes in biological material for decades. Over this period, cryo-LM has evolved from setups where the sample, the microscope, and the observer were put in an ice box, to sophisticated computer-controlled cryo stages that fit directly onto a regular microscope stage (for reviews, see (McGrath, 1987) and (Echlin, 1992). To the best of our knowledge, Makita et al. published in 1980 the first setup that allowed imaging of frozen hydrated material in liquid nitrogen (Makita et al., 1980). Their setup consisted of a liquid nitrogen bath that was mounted on a fluorescence microscope stage and in which a microscope objective was immersed. In our initial attempts to build a cryo-fluorescence system we also immersed the microscope objective in liquid nitrogen, but found that it caused persistent bubbling of the liquid nitrogen and thereby hampered image formation (not shown). Furthermore, the immersion of standard microscope objectives in liquid nitrogen is likely to cause lens aberrations leading to poor image quality.

Recently, two cryo-LM stages for the study of frozen-hydrated samples have been described that obviate the need for immersion of the microscope objective in liquid nitrogen (Sartori et al., 2007; Schwartz et al., 2007). Schwartz et al. (2007) aimed at developing a basic cryo-fluorescence microscope that should maintain the vitrified state of the specimen and prevent ice contamination from ambient air. Their system is mounted on an upright light microscope, operates at temperatures down to -140˚C, and has an estimated resolution of 0.6 µm. The cryo stage of Sartori et al. mounts on an inverted light microscope, yields fluorescent images with a lower resolution of 1.1 µm, but keeps the specimen at liquid nitrogen temperature. In addition, the authors describe a coordinate translation method for the quick retrieval in cryo-EM of previously identified fluorescent structures.

Building on the work done in the papers mentioned above, we chose to develop a self-contained cryo-FM workflow that i) can easily be implemented, ii) yields a higher optical resolution suitable for the detection of subcellular features, and iii) provides a user friendly and fast method to retrieve specific fluorescent structures in subsequent cryo-EM. The simplicity of our approach lies in the use of a commercially available freezing stage as the basis for the cryo-FM setup. To allow viewing of EM grids, we only modified the specimen cartridge, whereas to allow loading of vitrified specimens, we adapted the holder-loading mechanism of the stage. All modifications require basic workshop tools, and can be completed within a day's work.

The specimen cartridge was fitted with a thin brass disc to support the EM specimen grid. This made it possible to secure the grid using the clamp mechanism of an EM specimen holder. In addition, the brass acted as a cold sink for the sample and thereby prevented devitrification during the transfer steps. By replacing the original glass support with a brass disc, it was not possible anymore to view samples using transmitted light. Sartori et al. used transmitted light to locate large ice crystals and make estimates of the local sample thickness (Sartori et al., 2007). In our hands, we did not experience any inconvenience by the lack of the transmitted light option because of the absence of large ice crystals and because the thin cell peripheries were readily recognized in epifluorescence mode. In addition, the grid bars and lettering of the finder grids were also detected by epifluorescence.

To attain a relatively high lateral resolution of the cryo-fluorescence imaging system, the optical path was kept free of glass windows that might cause optical aberrations, and a dry objective without coverslip correction was selected that represented the best possible compromise between numerical aperture (0.75) and working distance (4.7 mm). The actual resolution we measured with this combination of characteristics was 0.4 µm. It permitted accurate localization and separation of subcellular structures such as mitochondria and exocytosis sites. This level of accuracy was essential for the subsequent retrieval and imaging of the same structures in cryo-EM mode. The theoretical maximum resolution that can be obtained with a diffraction-limited imaging system using dry objectives is in the order of 0.3 µm, which is 0.1 µm better than the performance of the system described here. Such a gain in resolution would yield only marginal improvements in the amount of subcellular detail that can be extracted from a biological sample. Furthermore, it would require the use of an objective with a much shorter working distance that jeopardizes the vitreous state of preservation of the sample. For these reasons, we feel that our setup is close to optimal for what can be achieved within the constraints of diffraction-limited cryo-fluorescence microscopy. Recent advances in non-diffraction-limited visible light and fluorescence microscopy will be likely to open new vistas for superresolution cryo-light microscopy applications (Lippincott-Schwartz and Manley, 2009).

The coordinate translation routine we developed allows for the quick retrieval in cryo-EM mode of previously identified fluorescent features, and avoids the need of electron beam irradiation. The software tool translates specific locations in a cryo-fluorescence micrograph into EM x- and y-coordinates with minimal input from the user, who only has to indicate by hand several obvious landmarks on the grid. It is therefore straightforward and user friendly. In addition, it has a high spatial positioning accuracy of 0.5 µm. Lucic et al. (Lucic et al., 2007) described a comparable routine for multimodal coordinate retrieval; they estimated the spatial positioning accuracy to be 1-3 µm. The disparity in accuracy between both routines can be largely ascribed to differences in spatial resolution of the cryo-fluorescence imaging setups; with a better resolution, one can locate a structure of interest more precisely, and the coordinate translation will be more exact.

In general, the single most important problem in cryo-CLEM is frost buildup from ambient air during cryo-light microscopy. For the largest part, this appears to occur while the sample is being shuttled in and out of the cryo stage. Because the cryo stage is airtight and purged with dry nitrogen gas, there is less risk of ice contamination when the specimen is inside the stage. By performing the specimen transfer in liquid nitrogen vapor using a simple Styrofoam box construction, we managed to eliminate deposition of larger ice crystals, i.e. contaminants that are visible by fluorescence microscopy. However, small, randomly distributed ice contaminants (< 100 nm) were still sometimes encountered. Because they were sparse, relatively electron lucent, and did not appear to interact with the vitreous sample, we did not experience any appreciable limitation by them.

Although the cryo-FM stage is an integral part of the cryo-CLEM workflow described herein, it may also be used as a standalone device to visualize fluorescent labels that cannot be cross-linked by chemical fixatives. Examples of such labels are certain membrane intercalating dyes, polar tracers, and fluorescent dextrans. In high throughput studies where only static information on the distribution of nonfixable dyes is relevant, cryo-immobilization followed by cryo-FM may be a viable alternative to live-cell imaging. Another potential standalone application for the cryo-FM stage is to take snapshots of the distribution of highly dynamic ions and their fluorescent chelators. Although certain types of chelators can be chemically fixed with EDC (Tymianski et al., 1997), instantaneous fixation of the whole ion-chelator complex can only be achieved with cryo-immobilization (Verhaeghe et al., 2008; Zierold, 1991). Following cryo-immobilization, it appears that the fluorescent chelators remain fluorescent, as shown for Fura-2 by Sartori et al. (2007). It remains to be established, however, whether ratiometric indicator dyes such as Fura-2 retain their ability to reflect ion concentrations. Although Sartori et al. (2007) imaged cryo-fluorescence from Fura-2 loaded neurites, they did not provide details on whether or not they monitored the Fura-2 fluorescence at a single excitation wavelength or by ratiometry.

The correlation between the SYTO 59 signal at the cryo-FM level and mitochondria at the cryo-EM level was unmistakable. Thus there should be hardly any need to use electron dense labels for supplementary detection in cryo-EM mode of structures with similar or larger dimensions than mitochondria. Only for structures that are substantially smaller than the cryo-FM resolution of 0.4 µm, and that are embedded in a subcellular environment crowded with disparate features, it may be advantageous to use an electron dense label. Semiconductor quantum dots would be perfect candidates because they are both fluorescent and electron dense and because they can be conjugated to various probes including antibodies (Giepmans et al., 2005; Nisman et al., 2004). However, it remains technically challenging and cumbersome to introduce quantum dots into cells by current methods for vital labeling (Luccardini et al., 2007; Medintz et al., 2005).

The cryo-CLEM workflow allowed us to select mitochondria in thin areas of HUVECs and generate electron tomograms of whole mitochondria. To our knowledge, this is the first time human mitochondria were investigated by cryo-electron tomography, and, given that they were studied in a primary cell line without harsh treatments like subcellular fractionation, one may assume they are representative of their natural state. Because whole mitochondria were imaged, huge amounts of data could be extracted even from single tomographic reconstructions. We found that the cristae mostly formed lamellar structures crossing the whole mitochondrion, and that cristae frequently fused together or with the inner boundary membrane. In agreement with the previous studies on isolated whole mitochondria, we show similar intermembrane distances and comparable molecular densities extending from the inner mitochondrial membrane that were identified as ATP synthases (Frank et al., 2002; Nicastro et al., 2000). Due to the molecular crowdedness in the human mitochondria, the molecules on the outside of the cristal membranes were less pronounced then the macromolecular densities we sometimes observed in the lumen of the cristae. At present, we have no information on the nature of these intra-luminal densities. Frank et al. (2002) have described comparable densities in the intermembrane space and given that this space is continuous with the lumen of the cristae, they may represent the same macromolecular complex.

A striking difference with previous studies of mitochondria concerns the openings of the cristae into the inter membrane space. We found that these openings could be either circular or elongated, even spanning a complete mitochondrion. For decades, mitochondrial cristae were described as folds in the inner mitochondrial membrane and hence thought to form slit-like connections with the intermembrane space (Palade, 1952). This model was subsequently contradicted by electron tomographic data that showed only small circular pores (Daems and Wisse, 1966; Frey and Mannella, 2000). These small pores were also observed in isolated mitochondria from a fungus and from rat liver using cryo-electron tomography (Frank et al., 2002; Nicastro et al., 2000). Whereas this paradigm shift with respect to membrane connections is now increasingly accepted by the scientific community, our tomograms show unmistakably examples of elongated slit-like openings. It has been suggested that these elongated junctions arise in apoptotic cells (Sun et al., 2007). However, the enlarged openings would be expected to pair with other ultrastructural changes that are not present in our case, such as swelling of cristae and vesiculation of mitochondria. Furthermore, the general ultrastructure of the cells gave us no reason to suspect that the HUVECs used herein were undergoing apoptosis. Another argument that could be raised against our finding is that the fluorescent labeling of the mitochondria may have caused ultrastructural changes in the mitochondrial membranes. However, we found similar slit-like openings in cryo-tomograms of unlabeled mitochondria. Therefore we suggest that, at least in some cell types, slit-like openings between the intermembrane space and cristal lumina can exist under normal physiological conditions. The diversity of opening sizes might have an effect on mitochondrial activity by modulating the diffusion rates of internal metabolites.

Accordingly, computer simulations suggest that the size of cristal junctions can influence the rate of ATP synthesis (Mannella, 2008; Mannella et al., 2001).

Recently, another study used cryo-CLEM of vitreous sections to visualize the ultrastructure of mammalian mitochondria (Gruska et al., 2008). The thinness of the samples, and therefore the lack of superimposed densities, gave rise to higher contrast and lateral resolution. Accordingly, macromolecular densities like ATP synthases were more easily distinguished than in whole mitochondria. On the other hand, the cryo-EM images of sectioned mitochondria showed artifacts that are common to cryo-sectioned material, like crevasses and uni-directional compression (Al-Amoudi et al., 2005; Dubochet et al., 2007).

Overall, in the current paper we have attempted to extend the value of cryo-CLEM by presenting a convenient and easily accessible workflow. It is suitable for a wide array of samples ranging from whole-mount cells to cryo-sectioned material to isolated cellular components. With regard to fluorescent labels, the system is pre-eminently suitable for correlating membrane permeable fluorescent dyes, surface labels, and genetic labels such as GFP.

Acknowledgements

The authors would like to thank Huybert van der Stadt and Bram de Visser from the technical workshop of the Leiden University Medical Center for their help in modifying the cryo-FM setup. We thank Erik Bos for technical assistance with the HUVEC cultures, and for video-taping the movie in supplementary material 1. We are grateful to Johan van der Vlist of FEI Company for kindly providing us with an EM grid holder. The 3D rendering of the THMS 600 freezing stage was kindly provided by Linkam Scientific. Lastly, we thank Montserrat Barcena for help with cryo-EM and Frank Faas for help with the resolution measurements. This work was supported by the EU within the Network of Excellence program on 3D-EM (www.3dem-noe.org).

Supplementary material can be found on the internet.

References

Abramoff, M.D., Magelhaes, P.J., Ram, S.J., 2004. Image Processing with ImageJ. Biophotonics International, pp. 36-42.

Agronskaia, A.V., Valentijn, J.A., van Driel, L.F., Schneijdenberg, C.T., Humbel, B.M., van Bergen En Henegouwen, P.M., Verkleij, A.J., Koster, A.J., and Gerritsen, H.C., 2008. Integrated fluorescence and transmission electron microscopy. J. Struct. Biol.

Al-Amoudi, A., Studer, D., and Dubochet, J., 2005. Cutting artefacts and cutting process in vitreous sections for cryo-electron microscopy. J. Struct. Biol. 150, 109-21.

Al-Amoudi, A., Chang, J.J., Leforestier, A., McDowall, A., Salamin, L.M., Norlen, L.P., Richter, K., Blanc, N.S., Studer, D., and Dubochet, J., 2004. Cryo-electron microscopy of vitreous sections. EMBO J. 23, 3583-8.

Babich, V., Meli, A., Knipe, L., Dempster, J.E., Skehel, P., Hannah, M.J., and Carter, T., 2008. Selective release of molecules from Weibel-Palade bodies during a lingering kiss. Blood 111, 5282-90.

Briegel, A., Ding, H.J., Li, Z., Werner, J., Gitai, Z., Dias, D.P., Jensen, R.B., and Jensen, G.J., 2008. Location and architecture of the Caulobacter crescentus chemoreceptor array. Mol. Microbiol. 69, 30-41.

Cyrklaff, M., Linaroudis, A., Boicu, M., Chlanda, P., Baumeister, W., Griffiths, G., and Krijnse-Locker, J., 2007. Whole cell cryo-electron tomography reveals distinct disassembly intermediates of vaccinia virus. PLoS ONE 2, e420.

Daems, W.T., and Wisse, E., 1966. Shape and attachment of the cristae mitochondriales in mouse hepatic cell mitochondria. J. Ultrastruct. Res. 16, 123-40.

Dubochet, J., Zuber, B., Eltsov, M., Bouchet-Marquis, C., Al-Amoudi, A., and Livolant, F., 2007. How to "read" a vitreous section. Methods Cell Biol. 79, 385-406.

Dubochet, J., Adrian, M., Chang, J.J., Homo, J.C., Lepault, J., McDowall, A.W., and Schultz, P., 1988. Cryo-electron microscopy of vitrified specimens. Q. Rev. Biophys. 21, 129-228.

Echlin, P., 1992. Low-Temperature Light Microscopy. Low-Temperature Microscopy and Analysis. Plenum Press, New York, pp. 265-293.

Frank, J., Wagenknecht, T., McEwen, B.F., Marko, M., Hsieh, C.E., and Mannella, C.A., 2002. Three-dimensional imaging of biological complexity. J. Struct. Biol. 138, 85-91.

Frey, T.G., and Mannella, C.A., 2000. The internal structure of mitochondria. Trends Biochem. Sci. 25, 319-24.

Giepmans, B.N., Deerinck, T.J., Smarr, B.L., Jones, Y.Z., and Ellisman, M.H., 2005. Correlated light and electron microscopic imaging of multiple endogenous proteins using Quantum dots. Nat Methods 2, 743-9.

Gruska, M., Medalia, O., Baumeister, W., and Leis, A., 2008. Electron tomography of vitreous sections from cultured mammalian cells. J. Struct. Biol. 161, 384-92.

Koning, R.I., and Koster, A.J., 2009. Cryo-electron tomography in biology and medicine. Ann Anat., doi:10.1016/j.aanat.2009.04.003

Koning, R.I., Zovko, S., Barcena, M., Oostergetel, G.T., Koerten, H.K., Galjart, N., Koster, A.J., and Mommaas, A.M., 2008. Cryo electron tomography of vitrified fibroblasts: microtubule plus ends in situ. J. Struct. Biol. 161, 459-68.

Koster, A.J., and Klumperman, J., 2003. Electron microscopy in cell biology: integrating structure and function. Nat Rev Mol Cell Biol Suppl, SS6-10.

Koster, A.J., Grimm, R., Typke, D., Hegerl, R., Stoschek, A., Walz, J., and Baumeister, W., 1997. Perspectives of molecular and cellular electron tomography. J. Struct. Biol. 120, 276-308.

Kremer, J.R., Mastronarde, D.N., and McIntosh, J.R., 1996. Computer visualization of three-dimensional image data using IMOD. J. Struct. Biol. 116, 71-6.

Kurner, J., Medalia, O., Linaroudis, A.A., and Baumeister, W., 2004. New insights into the structural organization of eukaryotic and prokaryotic cytoskeletons using cryo-electron tomography. Exp. Cell Res. 301, 38-42.

Leis, A., Rockel, B., Andrees, L., and Baumeister, W., 2008. Visualizing cells at the nanoscale. Trends Biochem. Sci.

Lippincott-Schwartz, J., and Manley, S., 2009. Putting super-resolution fluorescence microscopy to work. Nat Methods 6, 21-3.

Luccardini, C., Yakovlev, A., Gaillard, S., van 't Hoff, M., Alberola, A.P., Mallet, J.M., Parak, W.J., Feltz, A., and Oheim, M., 2007. Getting across the plasma membrane and beyond: intracellular uses of colloidal semiconductor nanocrystals. J Biomed Biotechnol 2007, 68963.

Lucic, V., Kossel, A.H., Yang, T., Bonhoeffer, T., Baumeister, W., and Sartori, A., 2007. Multiscale imaging of neurons grown in culture: from light microscopy to cryo-electron tomography. J. Struct. Biol. 160, 146-56.

Makita, T., Hatsuoka, M., Watanabe, J., Sasaki, K., and Kiwaki, S., 1980. Fluorescence Microscopy of Hydrated Frozen-Sections under Liquid-Nitrogen. Cryo-Letters 1, 438-444.

Mannella, C.A., 2008. Structural diversity of mitochondria: functional implications. Ann. N. Y. Acad. Sci. 1147, 171-9.

Mannella, C.A., Pfeiffer, D.R., Bradshaw, P.C., Moraru, II, Slepchenko, B., Loew, L.M., Hsieh, C.E., Buttle, K., and Marko, M., 2001. Topology of the mitochondrial inner membrane: dynamics and bioenergetic implications. IUBMB Life 52, 93-100.

Marko, M., Hsieh, C., Schalek, R., Frank, J., and Mannella, C., 2007. Focused-ion-beam thinning of frozen-hydrated biological specimens for cryo-electron microscopy. Nat Methods 4, 215-7.

McGrath, J.J., 1987. Temperature-controlled cryogenic light microscopy - an introduction to cryomicroscopy. In: Grout, B.W.W., Morris, G.J. (Eds.), The Effects of Low Temperature on Biological Systems. Edward Arnold, London, pp. 234-267.

Medintz, I.L., Uyeda, H.T., Goldman, E.R., and Mattoussi, H., 2005. Quantum dot bioconjugates for imaging, labelling and sensing. Nat Mater 4, 435-46.

Nicastro, D., Frangakis, A.S., Typke, D., and Baumeister, W., 2000. Cryo-electron tomography of neurospora mitochondria. J. Struct. Biol. 129, 48-56.

Nisman, R., Dellaire, G., Ren, Y., Li, R., and Bazett-Jones, D.P., 2004. Application of quantum dots as probes for correlative fluorescence, conventional, and energy-filtered transmission electron microscopy. J. Histochem. Cytochem. 52, 13-8.

Palade, G.E., 1952. The fine structure of mitochondria. Anat. Rec. 114, 427-51.

Romani de Wit, T., Rondaij, M.G., Hordijk, P.L., Voorberg, J., and van Mourik, J.A., 2003. Real-time imaging of the dynamics and secretory behavior of Weibel-Palade bodies. Arterioscler. Thromb. Vasc. Biol. 23, 755-61.

Sartori, A., Gatz, R., Beck, F., Rigort, A., Baumeister, W., and Plitzko, J.M., 2007. Correlative microscopy: bridging the gap between fluorescence light microscopy and cryo-electron tomography. J. Struct. Biol. 160, 135-45.

Schwartz, C.L., Sarbash, V.I., Ataullakhanov, F.I., McIntosh, J.R., and Nicastro, D., 2007. Cryo-fluorescence microscopy facilitates correlations between light and cryo-electron microscopy and reduces the rate of photobleaching. J. Microsc. 227, 98-109.

Sun, M.G., Williams, J., Munoz-Pinedo, C., Perkins, G.A., Brown, J.M., Ellisman, M.H., Green, D.R., and Frey, T.G., 2007. Correlated three-dimensional light and electron microscopy reveals transformation of mitochondria during apoptosis. Nat Cell Biol 9, 1057-65.

Tymianski, M., Bernstein, G.M., Abdel-Hamid, K.M., Sattler, R., Velumian, A., Carlen, P.L., Razavi, H., and Jones, O.T., 1997. A novel use for a carbodiimide compound for the fixation of fluorescent and non-fluorescent calcium indicators in situ following physiological experiments. Cell Calcium 21, 175-83.

Valentijn, J.A., van Driel, L.F., and Koster, A.J., 2009. Correlative Light and Electron Microscopy: Getting the Best of Two Worlds. In: Salzer, R. (Ed.), Biomedical Imaging: Principals and Applications. Wiley-Interscience.

Valentijn, J.A., van Driel, L.F., Agronskaia, A.V., Knoops, K., Koning, R.I., Barcena, M., Gerritsen, H.C., and Koster, A.J., 2008. Novel Methods for Cryo-Fluorescence Microscopy Permitting Correlative Cryo-Electron Microscopy. Microscopy and Microanalysis 14, 1314-1315.

Valentijn, K.M., Valentijn, J.A., Jansen, K.A., and Koster, A.J., 2008. A new look at Weibel-Palade body structure in endothelial cells using electron tomography. J Struct Biol 161, 447-58.

van Driel, L.F., Knoops, K., Koster, A.J., and Valentijn, J.A., 2008. Fluorescent labeling of resin-embedded sections for correlative electron microscopy using tomography-based contrast enhancement. J. Struct. Biol. 161, 372-83.

Verhaeghe, E.F., Fraysse, A., Guerquin-Kern, J.L., Wu, T.D., Deves, G., Mioskowski, C., Leblanc, C., Ortega, R., Ambroise, Y., and Potin, P., 2008. Microchemical imaging of iodine distribution in the brown alga Laminaria digitata suggests a new mechanism for its accumulation. J Biol Inorg Chem 13, 257-69.

Vicidomini, G., Gagliani, M.C., Canfora, M., Cortese, K., Frosi, F., Santangelo, C., Di Fiore, P.P., Boccacci, P., Diaspro, A., and Tacchetti, C., 2008. High data output and automated 3D correlative light-electron microscopy method. Traffic 9, 1828-38.

Zierold, K., 1991. Cryofixation methods for ion localization in cells by electron probe microanalysis: a review. J. Microsc. 161, 357-66.

Supplementary Material 1: Video recording illustrating the transfer of an EM specimen grid into the cryo-FM specimen cartridge, and into the cryo-FM stage.

Supplementary Material 2: Further information on FM- to EM- coordinate translation using the home made software script LCOTRAS.

Supplementary Material 3: Movie of the cryo-tomogram and 3D model of the mitochondrion shown in Figure 7. Note that the junctions of the cristae with the inner boundary membrane are either small and circular, or elongated and spanning the whole mitochondrion.

Supplementary Material 4: Cryo-electron tomogram of a whole mitochondrion in a cultured mouse embryonic fibroblast. No fluorescent label was used. As in the labeled HUVECs, an elongated opening between cristal lumina and the intermembrane space can be seen. The slit-like opening has been modeled. A digital slice of this tomogram has been reproduced in Koning and Koster (2009).